BNL-225760-2024-JAAM

IS-ECG-3

Rational optimization of substituted α-MnO2 cathode for aqueous zinc-ion battery

T. Le, P. Liu

To be published in "Energy Storage"

June 2024

Chemistry Department

Brookhaven National Laboratory

U.S. Department of Energy

USDOE Office of Science (SC), Basic Energy Sciences (BES)

Notice: This manuscript has been authored by employees of Brookhaven Science Associates, LLC under Contract No.DE-SC0012704 with the U.S. Department of Energy. The publisher by accepting the manuscript for publication acknowledges that the United States Government retains a non-exclusive, paid-up, irrevocable, world-wide license to publish or reproduce the published form of this manuscript, or allow others to do so, for United States Government purposes.

DISCLAIMER

This report was prepared as an account of work sponsored by an agency of the United States Government. Neither the United States Government nor any agency thereof, nor any of their employees, nor any of their contractors, subcontractors, or their employees, makes any warranty, express or implied, or assumes any legal liability or responsibility for the accuracy, completeness, or any third party's use or the results of such use of any information, apparatus, product, or process disclosed, or represents that its use would not infringe privately owned rights. Reference herein to any specific commercial product, process, or service by trade name, trademark, manufacturer, or otherwise, does not necessarily constitute or imply its endorsement, recommendation, or favoring by the United States Government or any agency thereof or its contractors or subcontractors. The views and opinions of authors expressed herein do not necessarily state or reflect those of the United States Government or any agency thereof.

Rational Optimization of Substituted α-MnO_2 Cathode for Aqueous Zinc-ion Battery

*Thanh Le[a], Esther S. Takeuchi[a,b,cd], Kenneth J. Takeuchi[a,b,c,e], Amy C. Marschilok[a,b,c,d], and Ping Liu[a,e]**

[a] Department of Chemistry, State University of New York at Stony Brook, Stony Brook, NY 11794

[b] Institute of Energy: Sustainability, Environment, and Equity (I:SEE), State University of New York at Stony Brook, Stony Brook, NY 11794

[c] Interdisciplinary Science Department, Brookhaven National Laboratory, Upton, NY 11973

[d] Department of Materials Science and Chemical Engineering, State University of New York at Stony Brook, Stony Brook, NY 11794

[e] Chemistry Division, Brookhaven National Laboratory, Upton, NY 11973

* Email: pingliu3@bnl.gov

KEYWORDS: hydrated zinc-ion batteries, hollandite α-MnO_2 cathode, optimization, vanadium and chromium substitution, discharge of proton/zinc, density functional theory

Abstract

Density functional theory (DFT) is utilized to explore the effects of increasing concentrations of vanadium (V) and chromium (Cr) substitution on the discharge of α-MnO_2 cathode in hydrated zinc-ion batteries (ZIBs). During H^+-intercalation and Zn^{2+}-intercalation, Cr-substitution proves to be more effective than V-substitution in promoting discharge behaviors. Transitioning from $Mn_{0.875}Cr_{0.125}O_2$, $Mn_{0.75}Cr_{0.25}O_2$ to $Mn_{0.625}Cr_{0.375}O_2$ is found to consistently enhance the discharge voltage, along with improved tunnel structure retention and volume expansion suppression. In comparison, the promoting effect of increasing V-substitution is relatively small at initial discharge stages and leads to degradation at later stages, primarily due to an increased concentration of unstable Mn^{2+} ion. The superior effect of Cr-substitution is attributed to the unique atomic and electronic structures of substituted Cr^{4+} and reduced Cr^{3+} ions during discharge. These ions serve as active electron acceptors to limit the formation of Mn^{3+} and Mn^{2+} ions, and as anchors to stabilize the α-MnO_2 framework and intercalated H^+/Zn^{2+} ions, respectively. Our study highlights fine-tuning through substitution to enhance the performance of α-MnO_2-based cathode materials in ZIBs.

1. Introduction

The quest for green and sustainable technologies has been significantly advanced by the development of lithium-ion batteries (LIBs). Despite their widespread use, LIBs face critical limitations, including flammability, high production costs, and limited lithium resources.[1] In response, both private and public sectors are intensifying efforts to explore rechargeable aqueous battery solutions that utilize non-flammable aqueous electrolytes as safer alternatives.[2-4] Rechargeable aqueous zinc-ion batteries (ZIBs) emerge as a highly promising option, thanks to their utilization of economically viable and water-compatible zinc ions, coupled with the exceptional anode material capabilities of zinc metal. [5, 6]

Tunnel-type hollandite, α-MnO_2, has shown compelling advantages as a cathode material in ZIB when used within a mildly acidic electrolyte, including cost-effective synthesis and high energy density.[4-10] However, the utility of α-MnO_2 is compromised by the structural degradation upon prolonged cycling associated with the irreversible partial dissolution of Mn^{2+} ions, and its optimization remains a challenge due to elusive mechanisms.[4, 5] The strategy of doping engineering has proven to be highly effective in improving both the structural integrity and the performance of cathode materials.[11] It has been reported that transition metals, including vanadium (V),[12] cobalt (Co),[13] and nickel (Ni),[14] are commonly used dopants, enhancing the structural stability and ZIB performances.

Our recent studies using density functional theory (DFT), in interaction with experiments, revealed the dynamic H^+-/Zn^{2+}-ion intercalation mechanism of α-MnO_2 in hydrated ZIB,[15-17] among several mechanisms proposed previously. [5, 7, 8, 18-29] Furthermore, the hydrated environment was found to play an essential role during discharge. This mechanistic understanding provides a strong basis for enhancing the ZIB performance by introducing the secondary transition metals (M= V or Cr) into of α-MnO_2, which prefer to substitute the Mn^{4+} ions ($Mn_{0.875}M_{0.125}O_2$) according to the DFT and transmission electron microscopic (TEM) studies.[16, 17] Notably, the substitutions, particularly $Mn_{0.875}Cr_{0.125}O_2$, demonstrate a promoting effect on structural stability, voltage, capacity retention, and cyclability during discharge.

Building upon our previous findings,[16] the current study aims to further elucidate the tuning behaviors of substitution during hydrated H^+- and Zn^{2+}-intercalation using DFT. The strategy is to increase the concentration of Cr^{4+} and V^{4+} substituent ions in α-MnO_2 and form $Mn_{0.75}M_{0.25}O_2$ and $Mn_{0.625}M_{0.375}O_2$. The elevated concentration of these metals in the 2 × 2 tunnels is hypothesized to enhance the electrochemical performance of $Mn_{1-z}M_zO_2$ in hydrated ZIBs. Indeed, the DFT results confirm that $Mn_{0.625}Cr_{0.375}O_2$ outperforms $Mn_{0.75}Cr_{0.25}O_2$ and $Mn_{0.875}Cr_{0.125}O_2$ by reducing the amount of $Mn^{\delta+}$ ion, particularly Mn^{2+} ion as a potential precursor for dissolution and phase separation. On the other hand, a higher concentration of V^{4+} ion results in a higher amount of unstable $Mn^{\delta+}$ ions, leading to more pronounced structural degradation and a reduction in discharge voltage. This study thus provides valuable insight and guidance for

effectively optimizing α-MnO_2-based cathodes by substitution to achieve enhanced discharge potential and capacity retention during continuous cycling in hydrated ZIBs.

2. Results and Discussion

2.1. Structures of Substituted $Mn_{0.75}M_{0.25}O_2$

Our prior theoretical and experimental studies confirmed the preferential substitution of 3d transition metal ions for the Mn^{4+} in the tunnel wall of α-MnO_2.[17] For $Mn_{0.875}M_{0.125}O_2$, substituting one out of eight Mn^{4+} ions in a 2 × 2 tunnel for a $M^{\delta+}$ ion was found to preserve the structural integrity of the tunnel while effectively mitigating volume expansion during discharge.[16, 17, 30] Building on this effort, DFT was employed here to explore the effect of increased concentration of M on the discharging behaviors of $Mn_{1-z}M_zO_2$.

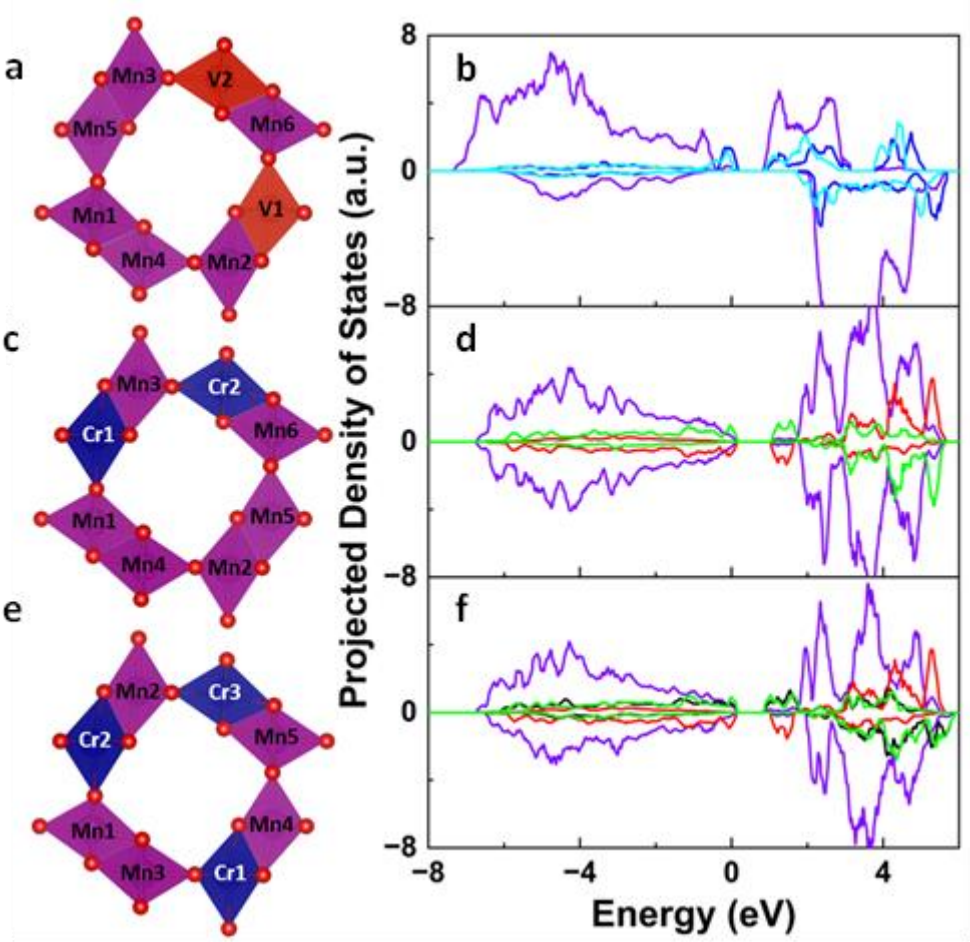

Figure 1. DFT-optimized structures of a) $Mn_{0.75}V_{0.25}O_2$, c) $Mn_{0.75}Cr_{0.25}O_2$, and e) $Mn_{0.625}Cr_{0.375}O_2$. The rectangle highlights the super cell considered in the DFT calculations. Red balls represent O atoms. Projected Density of States (PDOS) of b) $Mn_{0.75}V_{0.25}O_2$, d) $Mn_{0.75}Cr_{0.25}O_2$, and f) $Mn_{0.625}Cr_{0.375}O_2$. The contributions from Mn (purple line), $V_{1\text{-}2}$ (V_1: blue line; V_2: cyan line), $Cr_{1\text{-}2}$ in $Mn_{0.75}Cr_{0.25}O_2$ (Cr_1: red line; Cr_2: green line), and $Cr_{1\text{-}3}$ in $Mn_{0.625}Cr_{0.375}O_2$ (Cr_1: black line; Cr_2: red line; Cr_3: green line), are included.

Upon transitioning from $Mn_{0.875}M_{0.125}O_2$ to $Mn_{0.75}M_{0.25}O_2$, a second $M^{\delta+}$ ion is introduced into the wall of a 2 × 2 tunnel. Different from $Mn_{0.875}M_{0.125}O_2$, more possible positions need to be considered for the additional $M^{\delta+}$ ion (Figures S1 and S2, Tables S1 and S2). The results reveal that both $Mn_{0.75}V_{0.25}O_2$ and $Mn_{0.75}Cr_{0.25}O_2$ systems preferentially position two M^{4+} ions to be one Mn^{4+} ion apart from each other, forming row of side-sharing Mn^{4+}-M^{4+} pairs aligned in a zigzag motif (Figures 1a and 1c). This arrangement significantly enhances the stability of the tunnel framework. According to the calculated partial density of states (PDOS) and Bader charge analysis, each substituted V^{4+} ion in $Mn_{0.75}V_{0.25}O_2$ acts as a shallow electron donor, dominating the highest occupied states (Figure 1b). In contrast, the Cr^{4+} ion in $Mn_{0.75}Cr_{0.25}O_2$ is an active electron acceptor, contributing to the lowest unoccupied states (Figure 1d). In both cases, the Mn^{4+} ions that interact directly with M^{4+} ions are stabilized, evidenced by a downshift of states near the Fermi level (Figures 1b and 1d). Compared to $Mn_{0.875}M_{0.125}O_2$,[16] the formation of zigzag Mn^{4+}-M^{4+} row in $Mn_{0.75}M_{0.25}O_2$ introduces more significant stabilization to the interacted Mn^{4+} ions and consequently the overall framework. As demonstrated below, the substitution-promoted stability was also observed during discharge.

2.2. Proton Intercalation of $Mn_{0.75}M_{0.25}O_2$

To capture the feasible changes induced by H^+-intercalation, we mapped the potential insertion sites for H^+ ions and determined the concentration and position of co-inserted water molecules in $Mn_{0.75}M_{0.25}O_2H_x•y(H_2O)$ (Figure 2). According to our previous studies,[15, 16] the configuration with the lowest formation energy was selected as the starting point for the subsequent intercalation, $Mn_{0.75}M_{0.25}O_2H_{x+1}•y(H_2O)$, as well as for analysis of the intercalation-induced structural changes and estimation of the discharge voltages. We note that at the same discharge state of x in $Mn_{0.75}M_{0.25}O_2H_x•y(H_2O)$, the amount of co-intercalated H_2O remains constant, independent of the type and concentration of the substituent, M. This allows us to gain a better understanding of the promoting effects introduced by the substituent, which is the primary objective of our study.

The variation in formation energy for $Mn_{0.75}M_{0.25}O_2H_x•y(H_2O)$ follows the same trend as the earlier findings for $Mn_{0.875}M_{0.125}O_2H_x•y(H_2O)$, where the stability of intermediate states declines with increasing levels of intercalation (Figure 3).[16] At $n \leq 0.25$ (n: the number of transferred electrons per $Mn_{0.75}M_{0.25}O_2$ during discharge), a clear enhancement in stability was observed when transitioning from $Mn_{0.875}V_{0.125}O_2H_x•y(H_2O)$ (E_f = -2.08 eV at x = 0.125, E_f = -2.01 eV at x = 0.25) to $Mn_{0.75}V_{0.25}O_2H_x•y(H_2O)$ (E_f = -2.28 eV at x = 0.125, E_f = -2.12 eV at x = 0.25, Figure 3a). However, the formation energies of these two systems converge quickly at $n \geq 0.375$. In comparison, the promoting effect induced by increasing Cr concentration is more significant. $Mn_{0.75}Cr_{0.25}O_2H_x•y(H_2O)$ is consistently more stable than $Mn_{0.875}Cr_{0.125}O_2H_x•y(H_2O)$, ranging from n = 0.125 (E_f = -2.80 eV vs. -2.50 eV) to n = 0.5, (E_f = -1.76 eV vs. -1.54 eV, Figure 3b). The energies start to converge till $n \geq 0.625$. Moreover, $Mn_{0.75}V_{0.25}O_2H_x•y(H_2O)$ demonstrates lower stability than $Mn_{0.75}Cr_{0.25}O_2H_x•y(H_2O)$, especially at $n \leq 0.5$ (Figure 3).

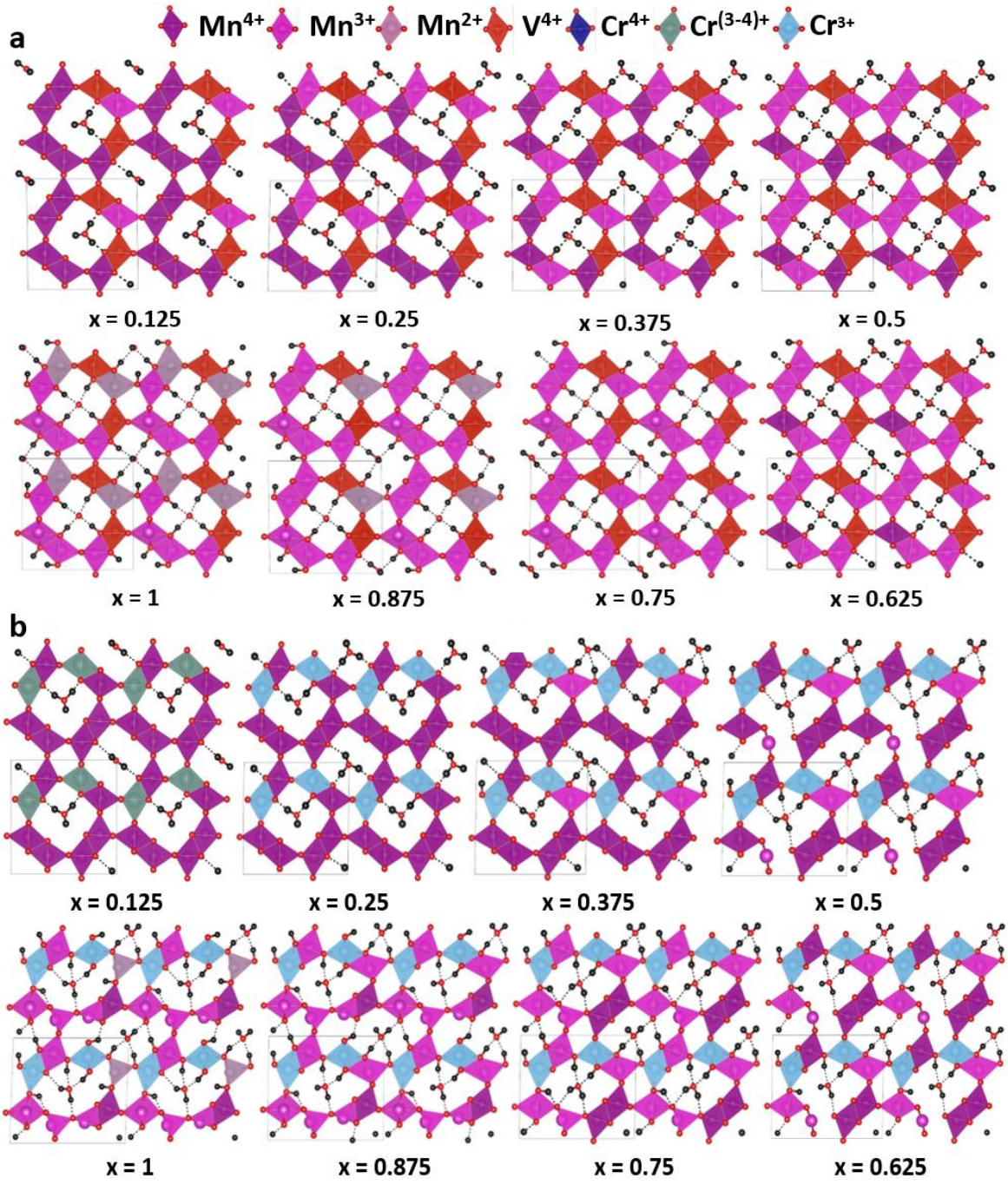

Figure 2. Optimized structures of a) $Mn_{0.75}V_{0.25}O_2H_x \bullet 0.25(H_2O)$ and b) $Mn_{0.75}Cr_{0.25}O_2H_x \bullet 0.25(H_2O)$. The rectangle highlights the supercell considered in the DFT calculations. Dotted lines represent hydrogen bonds. Black and red balls represent H and O atoms, respectively. The oxidation states of metal ions are labeled according to the Bader charge analysis.

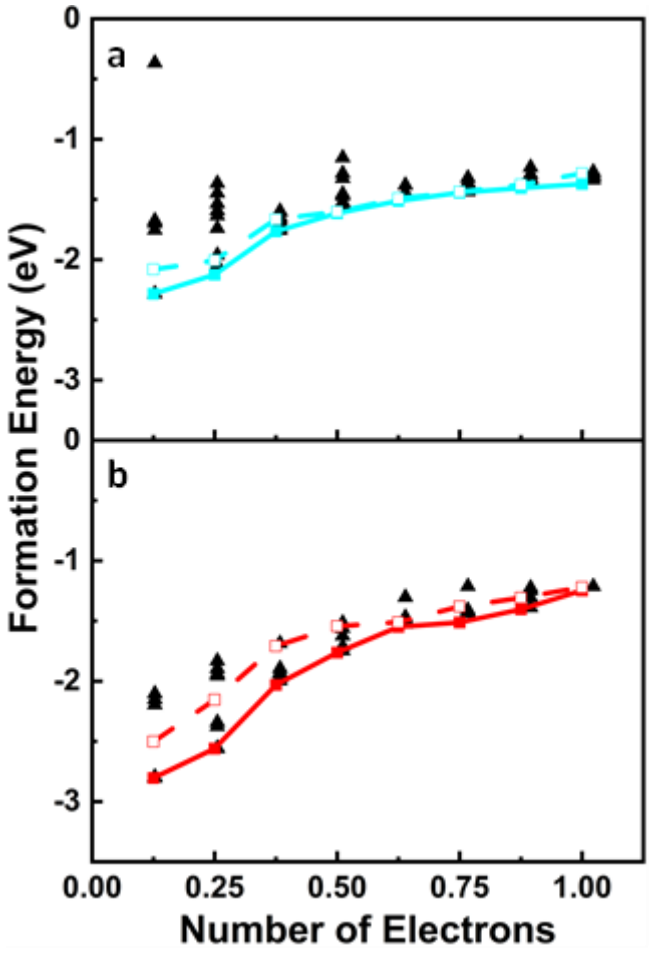

Figure 3. Calculated formation energies of a) $Mn_{0.75}V_{0.25}O_2H_x$•0.25(H_2O) (solid cyan line with solid cyan squares) and b) $Mn_{0.75}Cr_{0.25}O_2H_x$•0.25(H_2O) (solid red line with solid red squares) based on Equation 2. The most stable structure at each discharge stage is represented by solid squares and connected by a solid line. Solid black triangles represent unstable structures. The formation energies of the most stable $Mn_{0.875}V_{0.125}O_2H_x$•0.25($H_2O$) (dashed cyan line with hollow cyan squares) and $Mn_{0.875}Cr_{0.125}O_2H_x$•0.25($H_2O$) (dashed red line with hollow red squares) are included for comparison.

To understand the tuning effect introduced by increased substitution on formation energy, we analyzed the corresponding evolution in atomic and electronic structures during H^+-intercalation. At n = 0.125, for both substituted systems the intercalated H^+ was found to preferentially co-insert with H_2O molecules, resulting in the formation of $Mn_{0.75}M_{0.25}O_2H_{0.125}$•0.25($H_2O$) (Figure 2). A notable difference compared to $Mn_{0.875}M_{0.125}O_2H_{0.125}$ [16] is that for $Mn_{0.75}M_{0.25}O_2H_{0.125}$•0.25($H_2O$) the intercalated H^+ favors forming hydronium (H_3O^+) at the 2b site of 2 × 2 tunnel rather than hydroxyl (-OH) with the oxygen sites on the tunnel wall. The substituted MO_6 octahedron is a strong anchor for the central H_3O^+ via two H_2O-H•••O hydrogen bonds (Figure 2). At n = 0.25, the additional H^+ prefers to occupy the neighboring 2 × 2

tunnel and forms -OH on the wall, which can be further stabilized via a hydrogen bond with an existing H_2O molecule at the 2b site.

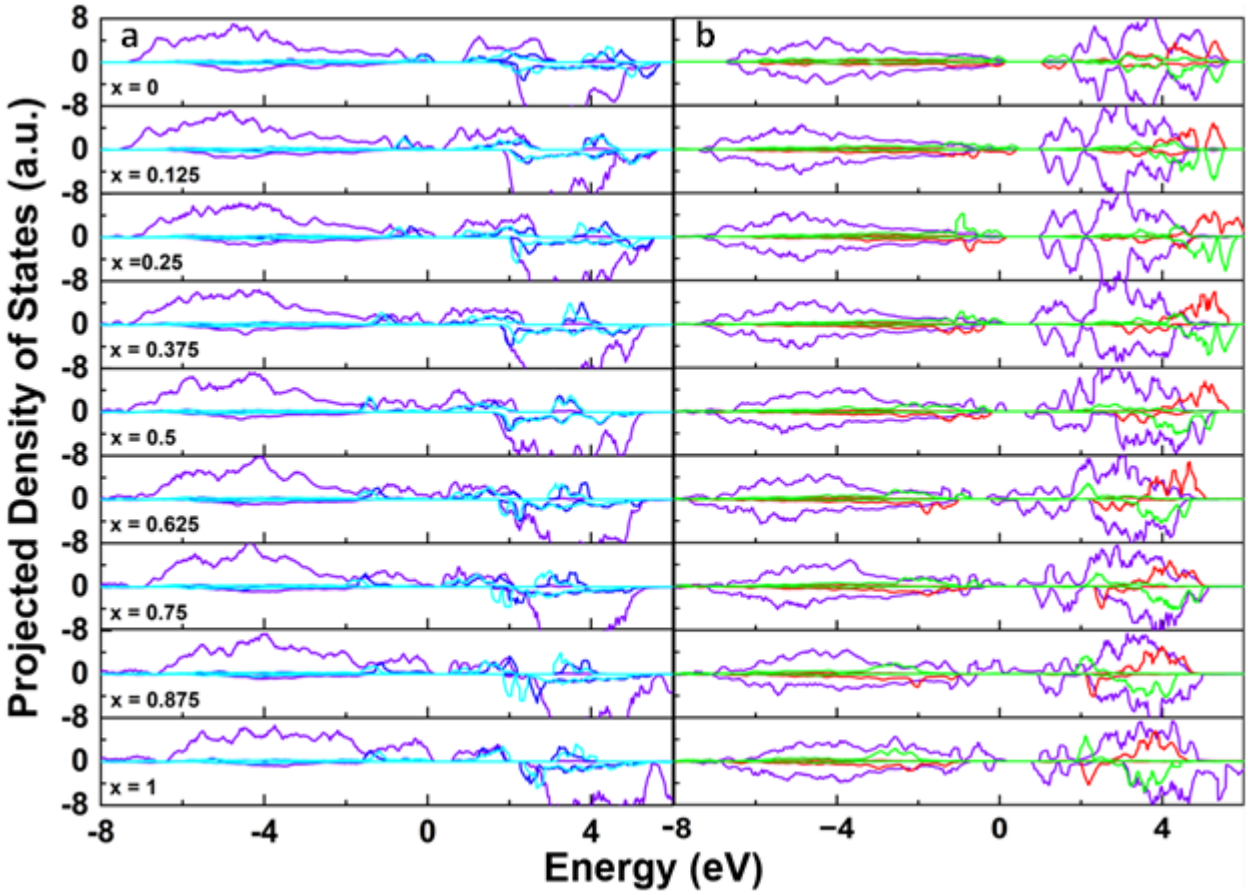

Figure 4. Projected Density of States of a) $Mn_{0.75}V_{0.25}O_2H_x$•0.25(H_2O) and b) $Mn_{0.75}Cr_{0.25}O_2H_x$•0.25(H_2O). The contributions from $Mn_{1\text{-}6}$ (purple line), $V_{1\text{-}2}$ (V_1: blue line; V_2: cyan line), and $Cr_{1\text{-}2}$ (Cr_1: red line; Cr_2: green line) are included. See Figure 1 for the labels of Mn, V, and Cr.

According to the calculated PDOS and Bader charge analysis, the lowest unoccupied states of $Mn_{0.75}V_{0.25}O_2$ are primarily contributed by Mn^{4+} rather than the substituted V^{4+} (Figure 4a). This suggests that Mn^{4+} is a less stable and can serve as a more active electron acceptor upon H^+-intercalation than V^{4+}. Indeed, 16.7% of Mn^{4+} is reduced to Mn^{3+} in $Mn_{0.75}V_{0.25}O_2H_{0.125}$•0.25($H_2O$) (Figure 2a). While the substituted V remains as 4+, consistent with our previous study of $Mn_{0.875}V_{0.125}O_2H_{0.125}$•0.25($H_2O$).[16, 17, 30] The difference is, however, each Mn^{3+} is more stabilized by the increased concentration of V-substitution via a V^{4+}-Mn^{3+}-V^{4+} motif (Figure 2a). Whereas, only one V^{4+} ion is in a direct contact with Mn^{3+} in $Mn_{0.875}V_{0.125}O_2H_{0.125}$.[16] As a result, the enhanced overlapping in state between Mn^{3+} and V^{4+} is observed (Figure 4a), stabilizing Mn^{3+} and thus overall structure (Figure 2a). The promoted stability by increased substitution is also demonstrated by the lattice change upon H^+-intercalation, where the volume expansion is rather

limited (4.8%) in $Mn_{0.75}V_{0.25}O_2H_{0.125}$•0.25($H_2O$), compared to that of $Mn_{0.875}V_{0.125}O_2H_{0.125}$•0.25($H_2O$) (5.6%, Figure 5).

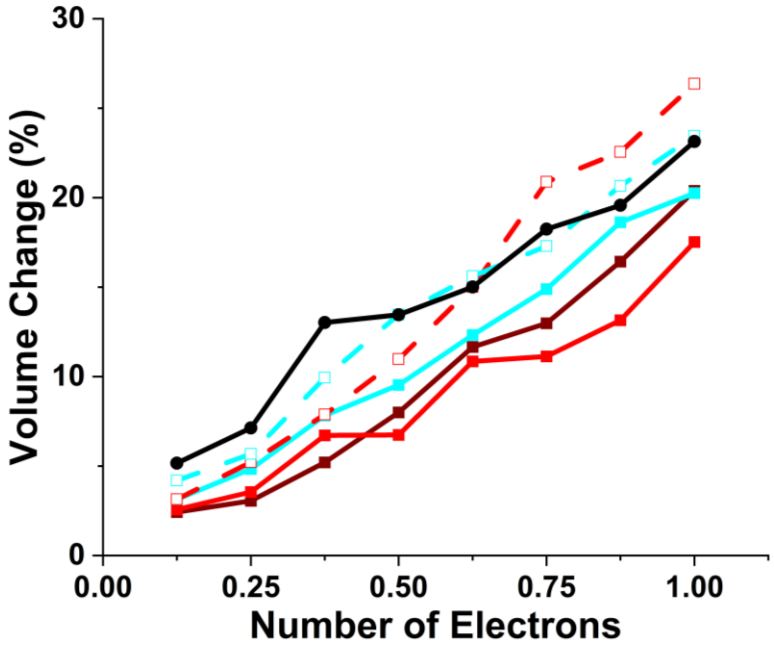

Figure 5. Variation in volume at different intercalation stages of MnO_2H_x•0.25(H_2O) (solid black line with solid black circles, cited[15]), $Mn_{0.875}V_{0.125}O_2H_x$•0.25($H_2O$) (dashed cyan line with hollow cyan squares, cited[16]), $Mn_{0.875}Cr_{0.125}O_2H_x$•0.25($H_2O$) (dashed red line with hollow red squares, cited[16]), $Mn_{0.75}V_{0.25}O_2H_x$•0.25(H_2O) (solid cyan line with solid cyan squares), $Mn_{0.75}Cr_{0.25}O_2H_x$•0.25(H_2O) (solid red line with solid red squares), and $Mn_{0.625}Cr_{0.375}O_2H_x$•0.25($H_2O$) (solid wine line with solid wine squares).

Conversely, with the dominant contribution to the lowest unoccupied states (Figure 4b), the substituted Cr^{4+} ion acts as an electron acceptor in $Mn_{0.75}Cr_{0.25}O_2$ and is more readily reduced on H^+-intercalation compared to Mn^{4+}, as observed in $Mn_{0.875}Cr_{0.125}O_2$.[16] At n = 0.25, all Cr^{4+} ions are reduced to 3+, while Mn ions remain as 4+ (Figure 2b). That is, the increased Cr-substitution via $Mn_{0.75}Cr_{0.25}O_2H_{0.25}$•0.25($H_2O$) completely avoids the formation of unstable Mn^{3+} at this stage, thus resulting in the enhanced stability and limited cell expansion (E_f = -2.56 eV; volume expansion = 3.5%) compared to $Mn_{0.875}Cr_{0.125}O_2H_{0.25}$•0.25($H_2O$) ($E_f$ = -2.15 eV; volume expansion = 5.2%) (Figures 3 and 5). While for $Mn_{0.75}V_{0.25}O_2H_{0.25}$•0.25($H_2O$), the promoting effect is less significant, where increased substitution does not affect the reduction of Mn^{4+} but imposing stabilization on reduced Mn^{3+}. In addition, $Mn_{0.75}Cr_{0.25}O_2H_{0.25}$•0.25($H_2O$) displays lower volume expansion and formation energies at n ≤ 0.25 than the V-substitution, which is consistent with the observation in $Mn_{0.875}M_{0.125}O_2H_x$•0.25($H_2O$) (Figures 3 and 5).

At n = 0.375, the existing central hydronium ions break down into water molecules and hydroxyl species (-OH) attached to the tunnel wall in both V- and Cr-substituted systems (Figure 2). Subsequent H^+ insertions up to n = 1 lead to hydroxylation of the 2 × 2 tunnel wall, which

interact with the central water molecule via hydrogen bonds. As seen for $Mn_{0.875}M_{0.125}O_2$,[16] during this process the concentration of unstable Mn^{3+} ions increases with increasing H^+ intercalation, instigating the significant structural distortion and volumetric expansion (Figures 2 and 5), as well as leading to a transition toward delocalization (Figure 4). Nevertheless, the tunnel structures remain during discharge.

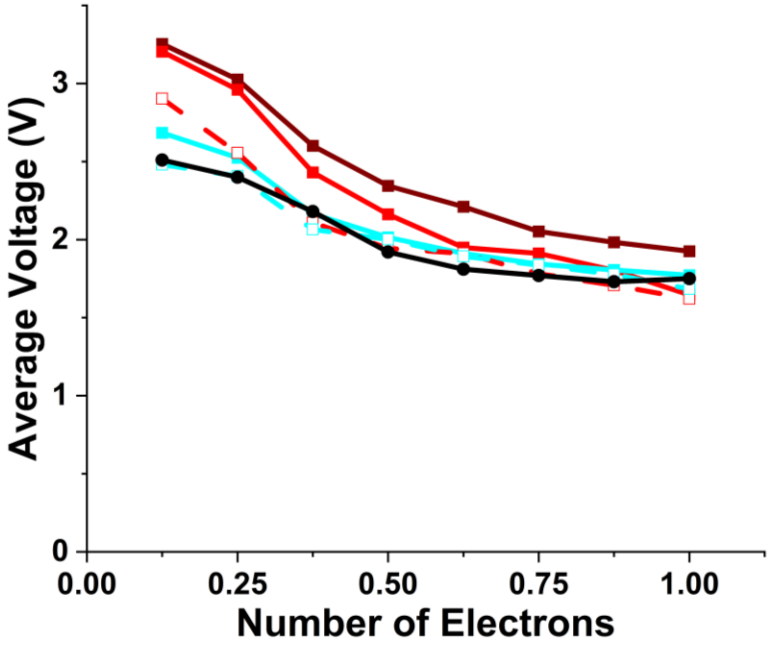

Figure 6. DFT-estimated discharge voltages of hydrated MnO_2H_x•0.25(H_2O) (solid black line with solid black circles, cited[15]), $Mn_{0.875}V_{0.125}O_2H_x$•0.25($H_2O$) (dashed cyan line with hollow cyan squares, cited[16]), $Mn_{0.875}Cr_{0.125}O_2H_x$•0.25($H_2O$) (dashed red line with hollow red squares, cited[16]), $Mn_{0.75}V_{0.25}O_2H_x$•0.25(H_2O) (solid cyan line with solid cyan squares), $Mn_{0.75}Cr_{0.25}O_2H_x$•0.25(H_2O) (solid red line with solid red squares), and $Mn_{0.625}Cr_{0.375}O_2H_x$•0.25($H_2O$) (solid wine line with solid wine squares).

The substitution on going from $Mn_{0.875}M_{0.125}O_2$ to $Mn_{0.75}M_{0.25}O_2$ shows an increasing promoting effect to pristine MnO_2, not only in limiting the cell expansion during discharge (Figure 5) but also in enhancing the discharge voltage (Figure 6). Compared to $Mn_{0.875}V_{0.125}O_2$, the possibility of forming unstable Mn^{3+} and Mn^{2+} in $Mn_{0.75}V_{0.25}O_2$ increases, which can potentially facilitate the tunnel breakage. While the substituted V is highly stable and remains as 4+ during H^+-intercalation, which helps to retain the tunnel structure (Figures 2a and 4a). As a result of compromise, the promotion by increasing V-substitution to $Mn_{0.75}V_{0.25}O_2$ is rather small in terms of cell retention and discharge voltage (Figures 5 and 6). In comparison, a more significant promotion was observed for substituted Cr^{4+}. Although Cr^{4+} is preferentially reduced to Cr^{3+} during discharge, Cr^{3+} is more stable than Mn^{3+} and Mn^{2+} by displaying higher unoccupied states in PDOS (Figure 4b) and remains as 3+ until n = 1 according to the Bader charge analysis. $Mn_{0.75}Cr_{0.25}O_2$ exhibits lower volume expansion during discharge compared to MnO_2, $Mn_{0.875}Cr_{0.125}O_2$, $Mn_{0.875}V_{0.125}O_2$, and $Mn_{0.75}V_{0.25}O_2$, with a volume expansion as low as 17.5% at

n = 1 (Figure 5). The superior suppression of cell expansion is associated with the unique promoting effect induced by increased substitution of Cr. As an active electron acceptor, it postpones the formation of Mn^{3+} to n = 0.375 and Mn^{2+} to n = 1 (Figure 2b). In addition, the reduced Cr^{3+} exerts additional stabilization on the tunnel structure by directly interacting with the unstable Mn^{3+} and Mn^{2+} ions (Figure 2b). Finally, the CrO_6 octahedron serves as an active anchoring site for H^+ ions inserted via preferential hydroxylation, which is more robust than VO_6 (Figure 2). According to the calculated discharge voltages based on the most stable H^+-intercalated intermediates identified (Figure 6), $Mn_{0.75}Cr_{0.25}O_2$ displays much higher discharge voltages than those of MnO_2, $Mn_{0.875}Cr_{0.125}O_2$, $Mn_{0.875}V_{0.125}O_2$, and $Mn_{0.75}V_{0.25}O_2$ at n ≤ 0.5. As n increases, the discharge voltages for these systems gradually decrease and begin to converge at n = 0.625 (Figure 6). The promoted discharge voltages resulting from increased Cr-substitution are more pronounced compared to those resulting from V-substitution. This effect is particularly notable at the early stages of the discharge, specifically at n ≤ 0.5.

2.3. Zinc Intercalation of $Mn_{0.75}M_{0.25}O_2$

The DFT calculations show a similar increase in formation energy of $Zn_xMn_{0.75}M_{0.25}O_2•y(H_2O)$ with the progressive Zn^{2+}-intercalation (Figure 7) as seen for H^{2+}-intercalation (Figure 3). While the change in energy is more pronounced for Zn^{2+}-intercalation. Compared to $Zn_xMn_{0.875}M_{0.125}O_2•y(H_2O)$,[16] the increase in substitution at each stage, again, helps to lower the formation energy, thereby promoting structural stability. In addition, $Zn_xMn_{0.75}Cr_{0.25}O_2•y(H_2O)$ outperforms $Zn_xMn_{0.75}V_{0.25}O_2•y(H_2O)$ by providing more stabilization to the intercalated Zn^{2+} ions and the intermediate states.

At n = 0.25, both substituted systems favor the co-insertion of a Zn^{2+} ion along with two dissociated and one molecular H_2O molecules, thereby forming $Zn_{0.125}Mn_{0.75}M_{0.25}O_2•0.375(H_2O)$ (Figure 8), which was also observed in $Zn_{0.125}Mn_{0.875}M_{0.125}O_2•0.375(H_2O)$.[16] The intercalated Zn^{2+} ion preferentially adopts a 4-coordinated 8h-like site to form $(OH)_2ZnO_2$ (Figure 8), as seen for α-MnO_2 and $Mn_{0.875}M_{0.125}O_2$, to improve the stability of the intercalated Zn^{2+} ions.[15, 16] Wherein, each Zn^{2+} ion is positioned at the center of the tetrahedron, with two corner oxygen atoms from the tunnel-wall and the other two from -OH fragments of dissociated H_2O. Consequently, the 2 × 2 tunnels that accommodate the intercalated Zn^+ ions experience significant distortion, leading to the tunnel breakage (Figure 8). The other H_2O molecule is located at the 2b site of the intact 2 × 2 tunnels. The produced mixed tunnel-layer structure with y = 0.375 is more stable than that with y = 0.125 and y = 0.25, where the tunnel structure remains intact.

Different from $Zn_{0.125}Mn_{0.875}M_{0.125}O_2•0.375(H_2O)$, a new position between two substituents in $Zn_{0.125}Mn_{0.75}M_{0.25}O_2•0.375(H_2O)$ was found to stabilize the intercalated Zn^{2+} ion well via a corner-sharing motif (Figure 8) and lower the formation energy significantly (Figure 7). This is accompanied by a two-electron transfer, which results in the reduction of 33.3% of Mn^{4+} ions to Mn^{3+} in the case of $Zn_{0.125}Mn_{0.75}V_{0.25}O_2•0.375(H_2O)$, while the substituted V ions remain intact in 4+ (Figures 7a, 8a and 9a). One type of the Mn^{3+} ions adopt a MnO_6 polyhedron and locates in the same layer as Zn^{2+}, allowing their direct interactions with both Zn^{2+} and neighboring

V^{4+} ions. The other type of Mn^{3+} prefer a MnO_4 polyhedron positioned in the opposite layer. With Cr-substitution, the substituted Cr^{4+} ions of $Zn_{0.125}Mn_{0.75}Cr_{0.25}O_2 \bullet 0.375(H_2O)$ contribute to the lowest unoccupied states of $Mn_{0.75}Cr_{0.25}O_2$ (Figure 9b) and are expected to be preferentially reduced at n = 0.25. Indeed, this is the case for 50% of Cr^{4+} ions. At meantime, 16.7% of Mn^{4+} is also reduced, which is associated with a MnO_4 polyhedron produced upon tunnel breakage, as seen in $Zn_{0.125}Mn_{0.75}V_{0.25}O_2 \bullet 0.375(H_2O)$ (Figure 8). Such low-coordinated Mn ions prefer to be reduced to 3+ together with the substituted Cr^{4+} (Figure 9b). In addition, owing to a lower concentration of unstable Mn^{3+} ions, the Cr-substituted systems are more stable than their V-substituted counterpart at n = 0.25.

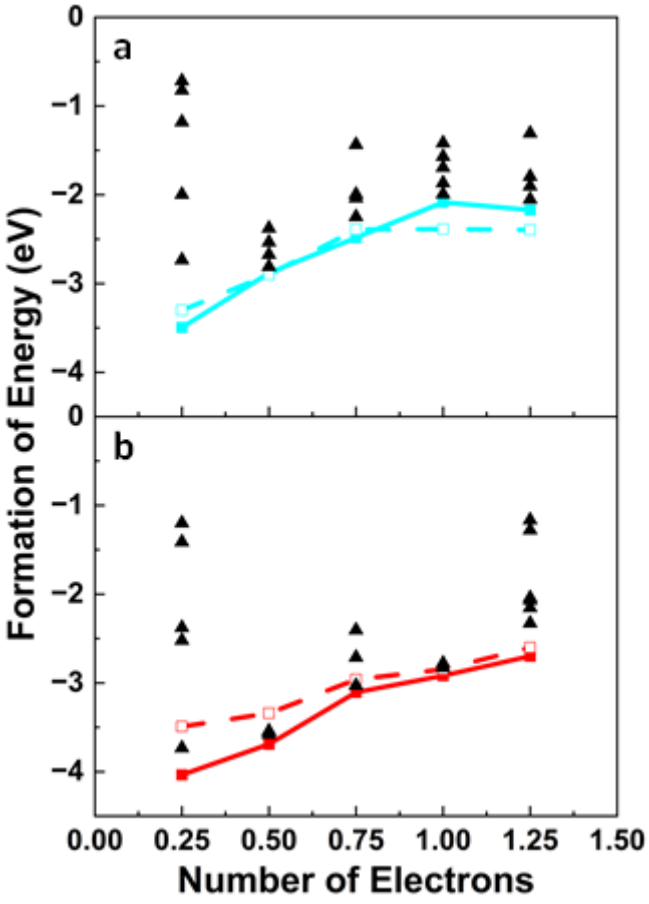

Figure 7. Calculated formation energies of a) $Zn_xMn_{0.75}V_{0.25}O_2 \bullet y(H_2O)$ (solid cyan line with solid cyan squares) and b) $Zn_xMn_{0.75}Cr_{0.25}O_2 \bullet y(H_2O)$ (solid red line with solid red squares) based on Equation 4. The most stable structure at each discharge stage is represented by solid squares and connected by a solid line. Solid black triangles represent unstable structures. The formation energies of $Zn_xMn_{0.875}V_{0.125}O_2 \bullet 0.25(H_2O)$ (dashed cyan line with hollow cyan squares) and $Zn_xMn_{0.875}Cr_{0.125}O_2 \bullet 0.25(H_2O)$ (dashed red line with hollow red squares) are included for comparison.

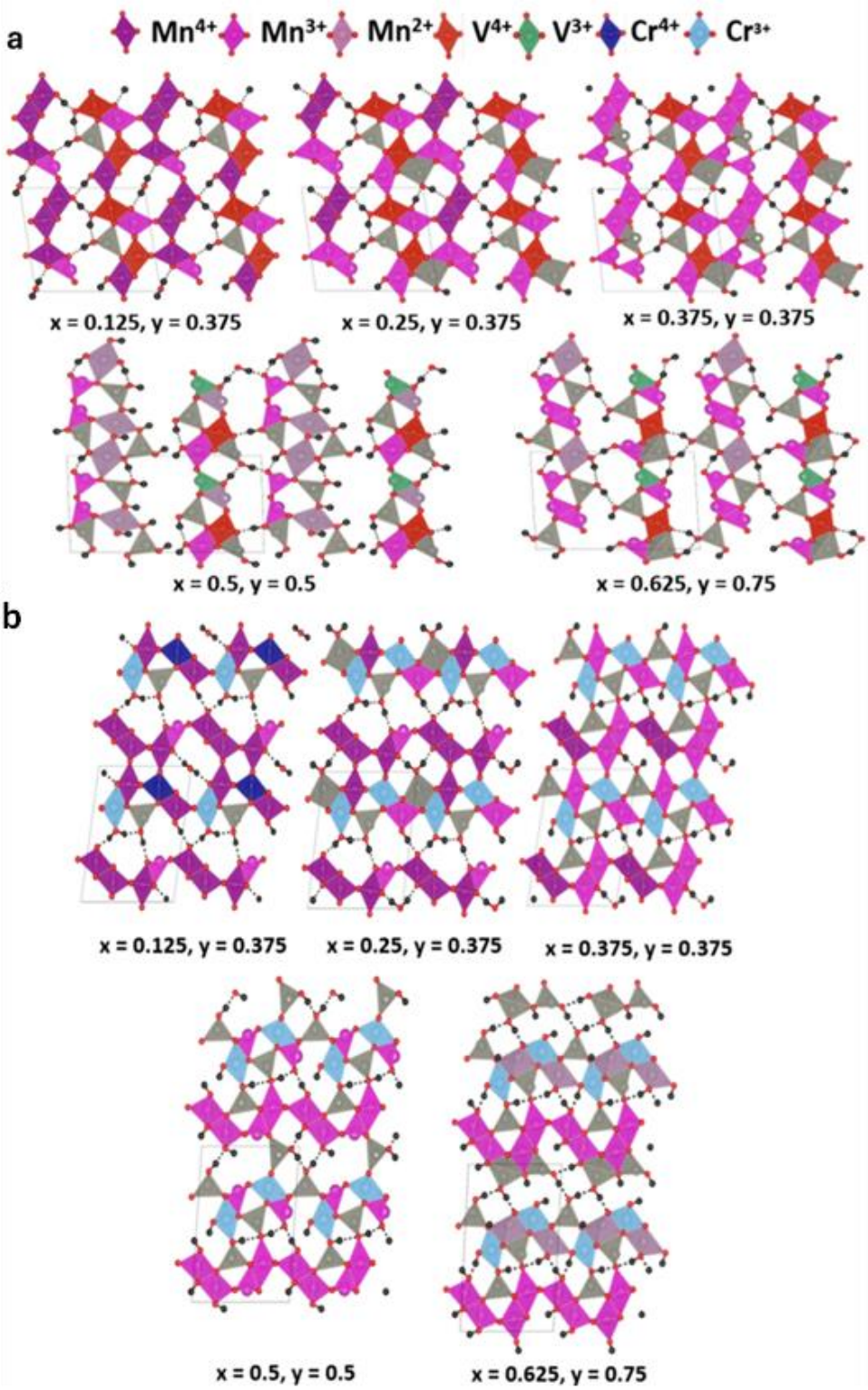

Figure 8. Optimized structures of a) $Zn_xMn_{0.75}V_{0.25}O_2 \bullet y(H_2O)$ and b) $Zn_xMn_{0.75}Cr_{0.25}O_2 \bullet y(H_2O)$. The rectangle highlights the super cell considered in the DFT calculations. Dotted lines represent hydrogen bonds. Black and red balls represent H and O atoms, respectively. The oxidation states of metal ions are labeled according to the Bader charge analysis.

Following the same mechanism as observed in $Mn_{0.875}M_{0.125}O_2$, additional Zn^{2+} ions intercalate into either the remaining 2 × 2 tunnels or the interspace between the existing layers of $Mn_{0.75}M_{0.25}O_2$. This process leads to a complete conversion from a mixed tunnel-layer structure, as observed at n = 0.25 to a complete layer-type structure, as observed at n = 1 (Figure 8). The subsequent intercalation at n ≥ 1 necessitates the insertion of additional H_2O molecules to serve as additional anchors. Nevertheless, the sequential Zn^{2+} intercalation is always associated with an increase in formation energy, indicating structural degradation (Figure 7).

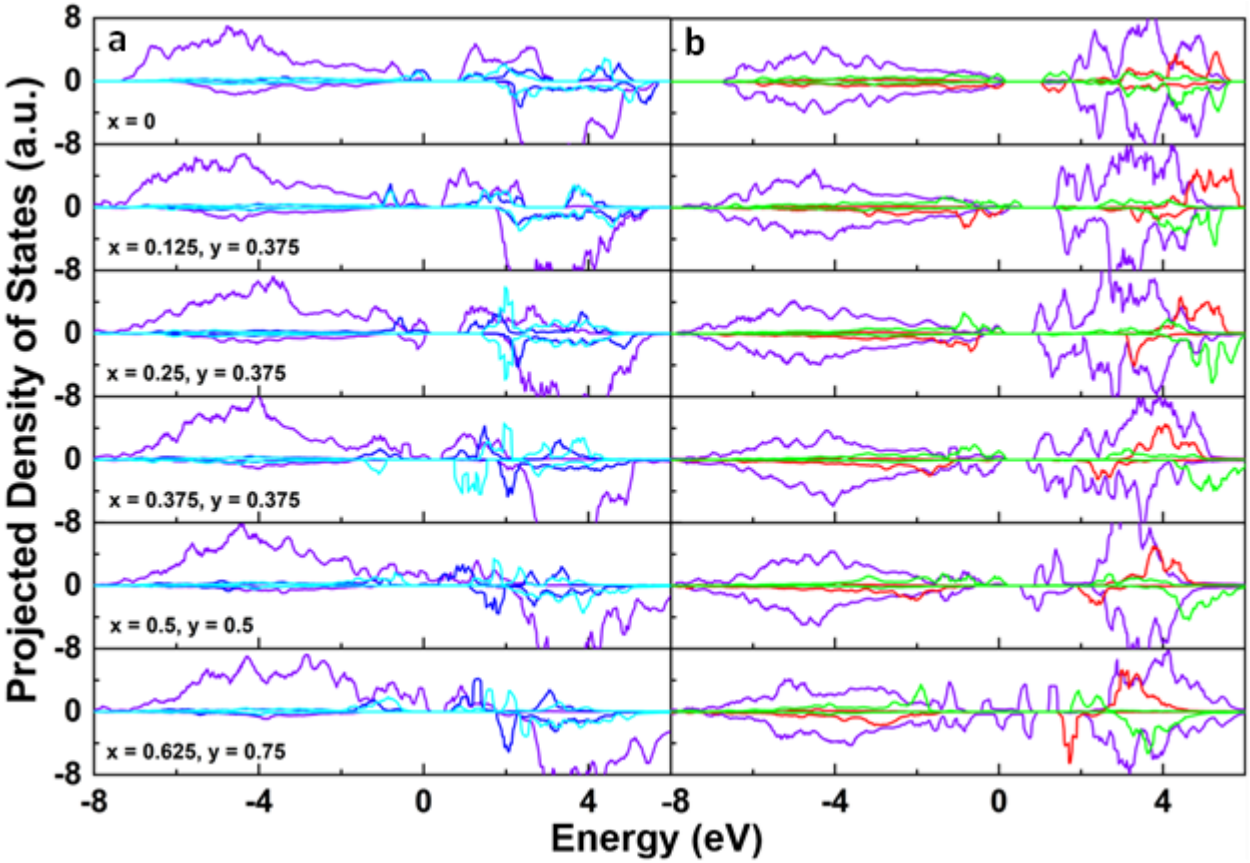

Figure 9. Projected Density of States of a) $Zn_xMn_{0.75}V_{0.25}O_2•y(H_2O)$ and b) $Zn_xMn_{0.75}Cr_{0.25}O_2•y(H_2O)$. The contributions from $Mn_{1\text{-}6}$ (purple line), $V_{1\text{-}2}$ (V_1: blue line; V_2: cyan line), and $Cr_{1\text{-}2}$ (Cr_1: red line; Cr_2: green line) are included. See Figure 1 for the labels of Mn, V, and Cr.

The promoting effect of increased Cr substitution is clearly demonstrated. Specifically, the formation energies of $Zn_xMn_{0.75}Cr_{0.25}O_2•y(H_2O)$ remain lower than $Zn_xMn_{0.875}Cr_{0.125}O_2•y(H_2O)$ during Zn^{2+}-intercalation. The gap in energy, though, narrows down as the intercalation advances, going from a maximum of 0.54 eV at n = 0.25 to a minimum of 0.10 eV at n = 1.25 (Figure 7b). In comparison, the effect of increased V-substitution is rather small. The formation energy of $Zn_xMn_{0.75}V_{0.25}O_2•y(H_2O)$ is higher than that of $Zn_xMn_{0.875}V_{0.125}O_2•y(H_2O)$ by 0.20 eV at n = 0.25, which overlaps at 0.5 ≤ n ≤ 0.75 and becomes lower by 0.12 eV at n = 1.25 (Figure 7a). That is,

increasing V-substitution in stabilizing Zn^{2+}-intercalated intermediates is not as effective as that observed for Cr-substitution. In addition, both $Zn_xMn_{0.875}Cr_{0.125}O_2•y(H_2O)$ and $Zn_xMn_{0.75}Cr_{0.25}O_2•y(H_2O)$ are more stable than the corresponding V-substituted systems at the same discharge state.

The less impact of increased V-substitution on formation energy compared to that of Cr-substitution can be well described by the associated changes in electronic structure. At n = 0.5, the intercalation of Zn^{2+}-intercalation leads to a complete reduction of Mn^{4+} ions to Mn^{3+} in $Zn_{0.25}Mn_{0.75}V_{0.25}O_2•0.375(H_2O)$ (Figures 8a and 9a). A reduction of V^{4+} to V^{3+} is also observed during a transition from n = 0.75 to n = 1, which does not occur during H^+-intercalation. This phenomenon is attributed to the substantial increase in structural distortion during Zn^{2+}-intercalation, leading to an enhanced contribution from V^{4+} ions to the lowest unoccupied states of $Zn_xMn_{0.75}V_{0.25}O_2•y(H_2O)$ and eventually the reduction V^{4+} to V^{3+} at n = 1 (Figures 8a and 9a). The presence of V^{3+} ions is evidenced by a morphological transition from VO_6 to VO_5 and from MnO_6 to MnO_4 for the neighboring $Mn^{\delta+}$ ions, together with the emergence of Mn^{2+} at n = 1. As a result, the associated tunnel is broken into a layer structure, leading to structural destabilization. Similar transition is also observed for $Zn_xMn_{0.875}V_{0.125}O_2•y(H_2O)$. Yet the induced structural changes are more substantial for $Zn_xMn_{0.75}V_{0.25}O_2•y(H_2O)$, which is well demonstrated by higher volume expansion by 5.9% at n = 0.75, 16.6% at n = 1, and 9.6% at n = 1.25 as compared to $Zn_xMn_{0.875}V_{0.125}O_2•y(H_2O)$ and $Zn_xMnO_2•y(H_2O)$ (Figure 10). The suppression of volume expansion on going from $Zn_xMn_{0.875}V_{0.125}O_2•y(H_2O)$ to $Zn_xMn_{0.75}V_{0.25}O_2•y(H_2O)$ is only seen at n < 0.5.

$Zn_xMn_{0.75}Cr_{0.25}O_2•y(H_2O)$ behaves differently from $Zn_xMn_{0.75}V_{0.25}O_2•y(H_2O)$. Each substituted $Cr^{\delta+}$ ion maintains a CrO_6 coordination and a side-sharing motif with neighboring $Mn^{\delta+}$ ions throughout the discharge process (Figure 8b). In addition, Mn^{2+} ions are not observed until n = 1.25 due to the preferential reduction of Cr^{4+}. This results in not only lower formation energies and higher stability of $Zn_xMn_{0.75}Cr_{0.25}O_2•y(H_2O)$ as compared to $Zn_xMn_{0.875}Cr_{0.125}O_2•y(H_2O)$, $Zn_xMn_{0.875}V_{0.125}O_2•y(H_2O)$, and $Zn_xMn_{0.75}Cr_{0.25}O_2•y(H_2O)$ (Figure 7), but also less volume expansion particularly at n > 0.5 (Figure 10). That is, a higher concentration of Cr ions can be advantageous in suppressing volume expansion at high discharge states, which is of great importance for promoting capacity and cyclability during discharge. Notably, the DFT-predicted volume change caused by Zn^{2+}-intercalation is too high at n > 0.75, when Mn^{2+} emerges and the structure undergo significant distortion (Figures 8 and 10). Such highly distorted structure likely acts as a precursor for decomposition, which cannot be captured by the DFT calculation and beyond the interest of current study. While the current focus is to demonstrate that the effect of substitution on suppressing the cell expansion at both early and late discharge stages.

The exceptional stabilization by the substituted $Cr^{\delta+}$ ion play a crucial role as opposed to the $V^{\delta+}$ counterpart in suppressing cell expansion. For instance, at n = 1, $Zn_{0.5}Mn_{0.75}Cr_{0.25}O_2•0.5(H_2O)$ does not contain any Mn^{2+} ions, which contributes to lower volume expansion than the counterpart V-substituted system, 43.2% vs. 56.9% (Figures 8b and 10). Even

as the discharge progresses to n = 1.25 and Mn^{2+} ions emerge, the volume expansion rate remains lower than in $Zn_{0.625}Mn_{0.75}V_{0.25}O_2$•0.75($H_2O$), 59.3% vs. 84.0%. In $Zn_{0.625}Mn_{0.75}Cr_{0.25}O_2$•0.75($H_2O$), all Mn^{2+} ions can interact with Cr^{3+} ions through an edge-sharing motif, while for $Zn_{0.625}Mn_{0.875}Cr_{0.125}O_2$•0.75($H_2O$), only 33.3% of Mn^{2+} ions can form bonds with Cr^{3+} and thus a higher expansion rate of 67.7% is observed (Figures 8b and 10). Notably, the newly formed layer in $Zn_{0.5}Mn_{0.75}V_{0.25}O_2$•0.5($H_2O$) exhibits an average interlayer distance of 5.84 Å, contributing to the observed the drastic volume expansion, whereas $Zn_{0.5}Mn_{0.75}Cr_{0.25}O_2$•0.5($H_2O$) maintains a shorter average distance of 4.89 Å and much lower cell expansion.

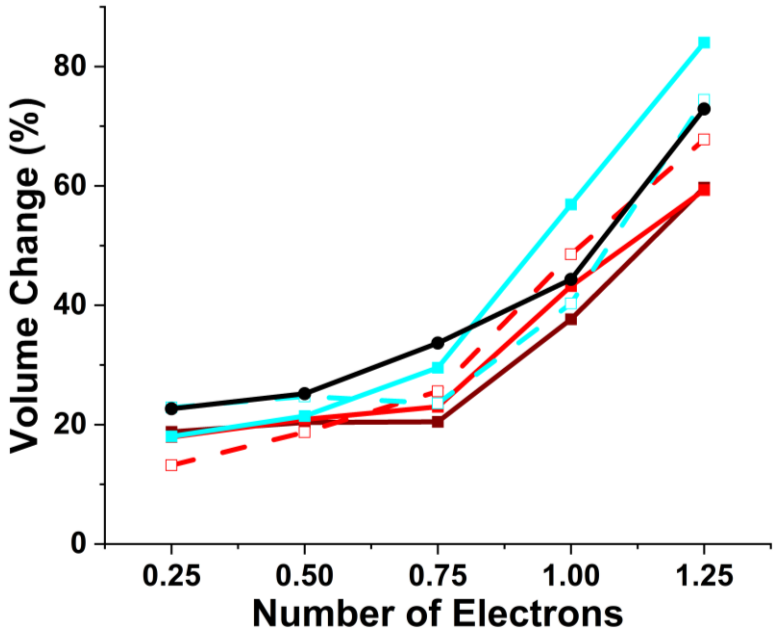

Figure 10. Variation in volume at different intercalation stages for Zn_xMnO_2•y(H_2O) (solid black line, cited[15]\), $Zn_xMn_{0.875}V_{0.125}O_2$•y($H_2O$) (dashed cyan line, cited[16]), $Zn_xMn_{0.875}Cr_{0.125}O_2$•y($H_2O$) (dashed cyan line, cited[16]), $Zn_xMn_{0.75}V_{0.25}O_2$•y(H_2O) (solid cyan line), $Zn_xMn_{0.75}Cr_{0.25}O_2$•y($H_2O$) (solid red line), and $Zn_xMn_{0.625}Cr_{0.375}O_2$•y($H_2O$) (solid wine line).

The promoting effect of increasing Cr-substitution is also observed for discharge voltage. Specifically, $Zn_xMn_{0.75}Cr_{0.25}O_2$•y($H_2O$) exhibits superior discharge voltages over Zn_xMnO_2•y(H_2O), $Zn_xMn_{0.875}V_{0.125}O_2$•y($H_2O$), $Zn_xMn_{0.875}Cr_{0.125}O_2$•y($H_2O$), and $Zn_xMn_{0.75}V_{0.25}O_2$•y(H_2O). This advantage is most pronounced at n = 0.25 with the difference in discharge voltage of 0.27 V, while it diminishes as n increases, reaching a minimal difference of 0.05 V at n = 1.25 (Figure 11). This is not observed by increasing V-substitution, which shows a subtle promotion on discharge voltage during the initial discharge (n ≤ 0.75) and even becomes detrimental at n ≥ 1. Specifically, $Zn_xMn_{0.875}V_{0.125}O_2$•y($H_2O$) shows higher discharge voltages than $Zn_xMn_{0.75}V_{0.25}O_2$•y(H_2O) by 0.31 V at n = 1 and 0.21 V at n = 1.25. In addition, both $Zn_xMn_{0.875}V_{0.125}O_2$•y($H_2O$) and $Zn_xMn_{0.75}V_{0.25}O_2$•y(H_2O) display lower discharge voltages than Zn_xMnO_2•y(H_2O) at n ≥ 0.5 (Figure 11). That is, despite the concentration of substituted $M^{\delta+}$ ions, Cr remains as a more effective substituent than V to enhance the discharge voltage of α-MnO_2. An interesting observation across

both substituted systems is the voltage plateau between n = 0.75 and n = 1. This plateau corresponds to the structural transition from a mixed layer-tunnel framework to a complete layered structure (Figure 11).

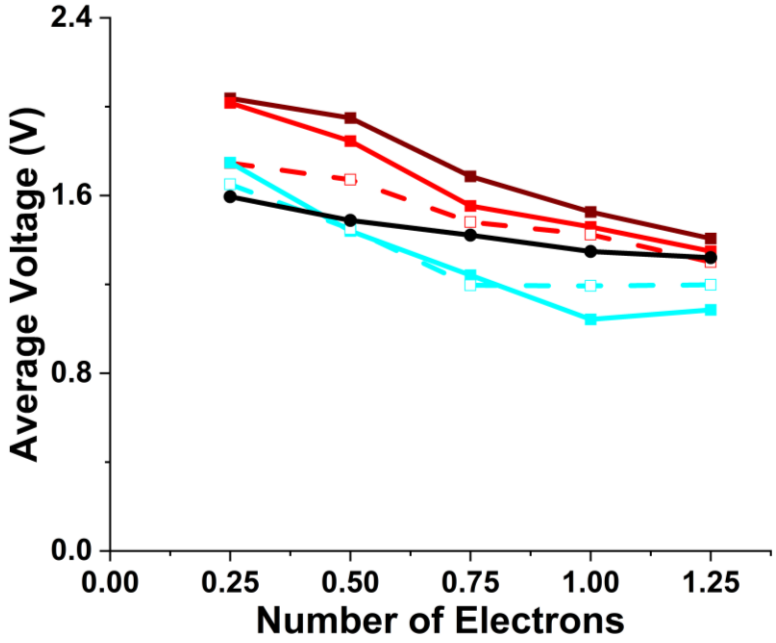

Figure 11. DFT-estimated discharge voltages during initial discharge of hydrated Zn_xMnO_2•y(H_2O) (solid black line, cited[15]), $Zn_xMn_{0.875}V_{0.125}O_2$•y($H_2O$) (dashed cyan line, cited[16]), $Zn_xMn_{0.875}Cr_{0.125}O_2$•y($H_2O$) (dashed red line, cited[16]), $Zn_xMn_{0.75}V_{0.25}O_2$•y(H_2O) (solid cyan line), $Zn_xMn_{0.75}Cr_{0.25}O_2$•y($H_2O$) (solid red line), and $Zn_xMn_{0.625}Cr_{0.375}O_2$•y($H_2O$) (solid wine line).

2.4. Behaviors of $Mn_{0.625}Cr_{0.375}O_2$

Motivated by the exceptional promoting effect observed for $Mn_{0.75}Cr_{0.25}O_2$ in enhancing voltage and mitigating volume expansion during H^+-/Zn^{2+}-intercalation (Figures 5, 6, 10 and 11), we now move to $Mn_{0.625}Cr_{0.375}O_2$, aiming to further increasing Cr-substitution and thus the impact on discharge performances. According to DFT calculations, the three substituted Cr ions in a 2 × 2 tunnel prefer to form three sets of edge-sharing Cr^{4+}-Mn^{4+} pairs and a Mn^{4+}-Mn^{4+} pair (Figures 1e and S3, Table S3).

The advantages of Cr^{4+} and reduced Cr^{3+} ions demonstrated during H^+-/Zn^{2+}-intercalation into $Mn_{0.75}Cr_{0.25}O_2$ are also observed for $Mn_{0.625}Cr_{0.375}O_2$, including the readily reduction of Cr^{4+} (Figure 1f) and additional stabilization imposed by Cr^{3+} (Figures S4-S7). Both $Mn_{0.625}Cr_{0.375}O_2H_x$•y($H_2O$) and $Zn_xMn_{0.625}Cr_{0.375}O_2$•y($H_2O$) exhibit a lower formation energy and higher structural stability compared to the counterparts with lower Cr-substitution during discharge (Figures S8 and S9). In addition, $Mn_{0.625}Cr_{0.375}O_2$ demonstrates a similarly low volume expansion on discharge as that of $Mn_{0.75}Cr_{0.25}O_2$ (Figures 5 and 10), while it provides a higher discharge voltage (Figures 6 and 11).

Among the α-MnO_2-based systems we studied,[15, 16] $Mn_{0.625}Cr_{0.375}O_2$ offers the highest discharge potential and the lowest volume expansion at highly discharged states (n > 0.5). These characteristics are key for enhancing both the capacity and cyclability of ZIBs. As we move from α-MnO_2 to $Mn_{0.875}Cr_{0.125}O_2$, $Mn_{0.75}Cr_{0.25}O_2$, and $Mn_{0.675}Cr_{0.375}O_2$, the gradual increase in Cr-substitution helps to stabilize the $Mn^{\delta+}$, H^+/Zn^{2+} ions that directly interacted and thus the overall framework during discharge, being able to provide a high discharge voltage with a relatively limited volume expansion (Figures 5, 6, 10 and 11). Our study demonstrates that introducing up to 37.5% Cr-substitution in α-MnO_2 can strategically enhance the structural stability and electrochemical performance during H^+- and Zn^{2+}-intercalation processes. The experimental validation of the DFT- predicted ZIB behaviors of $Mn_{1-x}M_xO_2$ is underway and will be reported later.

3. Conclusion

DFT calculations were utilized to investigate the impact of increasing V- and Cr-substitution on H^+- and Zn^+-intercalation in hydrated ZIBs using α-MnO_2 as a cathode material. It was clearly demonstrated that Cr-substitution is more effective than V-substitution in terms of promoting discharge voltage, retention of cell expansion and thus cyclability and capacity. During H^+-intercalation, the tunnel structure remains for all the systems studied. While $Mn_{0.625}Cr_{0.375}O_2$ consistently delivers the highest discharge voltages, which is followed by $Mn_{0.75}Cr_{0.25}O_2$ > $Mn_{0.75}Cr_{0.125}O_2$ > $Mn_{0.75}V_{0.25}O_2$ > $Mn_{0.75}V_{0.125}O_2$ in a decreasing sequence, along with the improved retention of the tunnel structure and the suppression of volume expansion. Superior promotion in performance by increased Cr-substitution of $Mn_{0.625}Cr_{0.375}O_2$ was also observed during Zn^{2+}-intercalation, though all systems undergo the tunnel to layer transition.

The superior promoting effect of Cr-substitution can be attributed to the unique atomic and electronic structures of substituted Cr^{4+} and reduced Cr^{3+} during discharge. The presence of Cr^{4+} ion enables preferential reduction over Mn^{4+} ions, thereby limiting the formation of unstable Mn^{3+} and Mn^{2+} centers. Furthermore, the resulted Cr^{3+} ion stabilizes not only the neighboring Mn^{3+}/Mn^{2+} ions via an edge-sharing conformation but also the intercalated H^+/Zn^{2+} ions. Among the systems studied, with the highest Cr-substitution $Mn_{0.625}Cr_{0.375}O_2$ enables the most significant enhancement in structural stability, being able to limit the structural distortion and volume expansion, maintain the active sites particularly at high discharge states, and eventually promote the discharge voltage, capacity, and cyclability. In comparison, the tuning by increasing V-substitution is rather poor, which is attributed to the increased concentration of Mn^{2+} ions and thus more pronounced structural degradation in discharge performance. Our study provides valuable insights on the fine-tuning by substitution in the performance of MnO_2-based electrodes in hydrated ZIBs. By selecting appropriate substituents with suitable concentrations, the electrochemical performance of the cathode can be effectively enhanced.

4. Computational Methods

Spin-polarized DFT calculations were conducted using the Vienna ab initio simulation package (VASP).[31-34] Following our previous studies,[15, 16] the treatment of core electrons was accomplished using the projector augmented wave (PAW) method with the Perdew-Burke-Ernzerhof (PBE) functionals within the generalized gradient approximation (GGA).[35, 36] The GGA functionals without van der Waals correction was found previously to well describe the chemical behaviors at the water-electrode interfaces observed experimentally.[37] The Kohn-Sham one-electron wave functions were expanded by employing a plane wave basis set with a kinetic energy cutoff of 650 eV. The Brillouin zone was sampled in the Monkhorst-Pack scheme.[38] The optimization of ionic positions was terminated when the Hellmann-Feynman force on each ion fell below 0.01 eV/Å. Soft potentials were employed for various elements, including H, O_GW, Mn_sv_GW, Cr_pv, V_pv, K_sv_GW, and Zn_sv_GW. A Hubbard correction with U = 5.1 eV and J = 1.2 eV was applied for Mn cations to reproduce the experimentally observed lattice constants and the antiferromagnetic nature of α-MnO_2.[39, 40] A supercell that consisted of 8 transition metal atoms and 16 oxygen atoms was used to model tetragonal α-MnO_2. The $Mn_{0.75}M_{0.25}O_2$ or $Mn_{0.625}M_{0.375}O_2$ systems were created by replacing Mn atoms on the tunnel wall, which led to the slight distortion in the lattice. Building upon our previous studies,[15, 16] a thorough examination was conducted for each intermediate state.

In order to quantify and compare the electrochemical performance of different systems, the average discharge voltage (V) for H^+-intercalation was expressed as[15, 16, 41]

$$V = -\frac{E(Mn_{1-z}M_zO_2H_x \bullet yH_2O) - E(Mn_{1-z}M_zO_2) - \frac{x}{2}E(H_2) - yE(H_2O)}{xF} \quad (1)$$

The formation energy (E_f) of H^+-intercalated intermediate was expressed as

$$E_f = \frac{E(Mn_{1-z}M_zO_2H_x \bullet yH_2O) - E(Mn_{1-z}M_zO_2) - \frac{x}{2}E(H_2) - yE(H_2O)}{x} \quad (2)$$

For Zn^{2+}-intercalation, the average discharge voltage was expressed as

$$V = -\frac{E(Zn_xMn_{1-z}M_zO_2 \bullet yH_2O) - E(Mn_{1-z}M_zO_2) - xE(Zn) - yE(H_2O)}{2xF} \quad (3)$$

And the formation energy was expressed as

$$E_f = \frac{E(Zn_xMn_{1-z}M_zO_2 \bullet yH_2O) - E(Mn_{1-z}M_zO_2) - xE(Zn) - yE(H_2O)}{x} \quad (4)$$

The DFT-calculated total energy of a specific system is denoted as E. x, y, and z represent the fractions of intercalated H^+ or Zn^{2+} ions, the co-intercalated H_2O molecules, and the substituted M in α-MnO_2. The Faraday constant is denoted as F. For the discharge voltage of each Zn^{2+} intercalation, we divided it by two since Zn^{2+} ions are bivalent.[42] Conversely, for H^+-intercalation, the discharge voltage was divided by one. Here, the decomposition of each discharged intermediate was not considered, which was associated with formation of Mn^{2+}, but evaluating the relative difference in stability from one state to another based on the calculated E_f. Note that the Zn/Zn^{2+} electrode was used as a reference electrode, and a correction of 0.40 V was

incorporated according to the Nernst equation to account for the contribution of H^+-intercalation at a pH of 6. Nevertheless, the current study is to identify the role of substitution in optimizing the discharge behavior of MnO_2. Thus, the difference from one system to the next is the interest, rather than the absolute value, which is difficult for quantitative comparison with the experiment.

The volume change during H^+-intercalation and Zn^{2+}-intercalation was expressed respectively as

$$\text{Volume Change} = \frac{V(H_xMn_{1-z}M_zO_2 \bullet yH_2O) - V(Mn_{1-z}M_zO_2)}{V(Mn_{1-z}M_zO_2)} \times 100\% \quad (5)$$

and

$$\text{Volume Change} = \frac{V(Zn_xMn_{1-z}M_zO_2 \bullet yH_2O) - V(Mn_{1-z}M_zO_2)}{V(Mn_{1-z}M_zO_2)} \times 100\% \quad (6)$$

The Bader analysis method was employed to determine the oxidation states of the metal ions during the discharge.[43-46] This analysis, combined with the calibration based on the reference oxidation states (Mn^{4+} of MnO_2, Mn^{3+} of Mn_2O_3, Mn^{2+} of MnO, Cr^{4+} of CrO_2, Cr^{3+} of Cr_2O_3, V^{4+} of VO_2, and V^{3+} of V_2O_3), was used to determine the oxidation states of the metal ions involved (Tables S4-S10). Additionally, the partial calculated density of states (PDOS) and magnetic moments were calculated. Wherein the decrease in oxidation states during the discharge is found to correlate with the increase in magnetic moment (Figures S10-S15).

Acknowledgement

This work was performed at Brookhaven National Laboratory and funded by the Center for Mesoscale Transport Properties (m2M), and Energy Frontier Research Center supported by the U.S. Department of Energy, Office of Science, Basic Energy Sciences, under award no. DE-SC0012673. The DFT calculations were carried out by utilizing the computational resources provided by the Center for Functional Nanomaterials at Brookhaven National Laboratory, a component of the Computational Science Initiative, at Brookhaven National Laboratory under contract no. DE-SC0012704, and Stony Brook Research Computing and Cyberinfrastructure and the Institute for Advanced Computational Science at Stony Brook University for access to the high-performance SeaWulf computing system, which was made possible by a $1.4M National Science Foundation grant (no. 1531492). EST acknowledges support as the William and Jane Knapp Chair in Energy and the Environment.

Conflict of Interest Statement

The authors declare no conflicts of interest.

Data Availability Statement

All data and code for this study are available upon request from the corresponding author.

References

[1] Q. Wang, P. Ping, X. Zhao, G. Chu, J. Sun, C. Chen. Thermal runaway caused fire and explosion of lithium ion battery. *Journal of power sources.* 2012; **208**: 210-224.
[2] F. Keck, M. Lenzen, A. Vassallo, M. Li. The impact of battery energy storage for renewable energy power grids in Australia. *Energy.* 2019; **173**: 647-657.
[3] W. A. Braff, J. M. Mueller, J. E. Trancik. Value of storage technologies for wind and solar energy. *Nature Climate Change.* 2016; **6**: 964-969.
[4] D. Davies, M. Verde, O. Mnyshenko, Y. Chen, R. Rajeev, Y. Meng, G. Elliott. Combined economic and technological evaluation of battery energy storage for grid applications. *Nature Energy.* 2019; **4**: 42-50.
[5] H. Pan, Y. Shao, P. Yan, Y. Cheng, K. S. Han, Z. Nie, C. Wang, J. Yang, X. Li, P. Bhattacharya. Reversible aqueous zinc/manganese oxide energy storage from conversion reactions. *Nature Energy.* 2016; **1**: 1-7.
[6] X. Jia, C. Liu, Z. G. Neale, J. Yang, G. Cao. Active materials for aqueous zinc ion batteries: synthesis, crystal structure, morphology, and electrochemistry. *Chemical Reviews.* 2020; **120**: 7795-7866.
[7] D. Wu, L. M. Housel, S. J. Kim, N. Sadique, C. D. Quilty, L. Wu, R. Tappero, S. L. Nicholas, S. Ehrlich, Y. Zhu. Quantitative temporally and spatially resolved X-ray fluorescence microprobe characterization of the manganese dissolution-deposition mechanism in aqueous Zn/α-MnO_2 batteries. *Energy & Environmental Science.* 2020; **13**: 4322-4333.
[8] X. Guo, J. Zhou, C. Bai, X. Li, G. Fang, S. Liang. Zn/MnO_2 battery chemistry with dissolution-deposition mechanism. *Materials Today Energy.* 2020; **16**: 100396.
[9] B. Wu, G. Zhang, M. Yan, T. Xiong, P. He, L. He, X. Xu, L. Mai. Graphene scroll-coated α-MnO2 nanowires as high-performance cathode materials for aqueous Zn-ion battery. Small. 2018; **14**: 1703850.
[10] X. Gao, H. Wu, W. Li, Y. Tian, Y. Zhang, H. Wu, L. Yang, G. Zou, H. Hou, X. Ji. H^+-insertion boosted α-MnO_2 for an aqueous Zn-ion battery. *Small.* 2020; **16**: 1905842.
[11] B. Zhang, J. Chen, W. Sun, Y. Shao, L. Zhang, K. Zhao. Challenges and perspectives for doping strategy for manganese-based zinc-ion battery cathode. *Energies.* 2022; **15**: 4698.
[12] M. H. Alfaruqi, S. Islam, V. Mathew, J. Song, S. Kim, D. P. Tung, J. Jo, S. Kim, J. P. Baboo, Z. Xiu. Ambient redox synthesis of vanadium-doped manganese dioxide nanoparticles and their enhanced zinc storage properties. *Applied Surface Science.* 2017; **404**: 435-442.
[13] Y. Tao, Z. Li, L. Tang, X. Pu, T. Cao, D. Cheng, Q. Xu, H. Liu, Y. Wang, Y. Xia. Nickel and cobalt Co-substituted spinel ZnMn2O4@ N-rGO for increased capacity and stability as a cathode material for rechargeable aqueous zinc-ion battery. *Electrochimica Acta.* 2020; **331**: 135296.
[14] J. Ji, J. Yao, Y. Xu, H. Wan, B. Zhang, L. Lv, J. Li, N. Wang, Z. Zheng, J. Zhang. Promoting Proton Migration Kinetics by Ni^{2+} Regulating Enables Improved Aqueous Zn-MnO_2 Batteries. *Energy & Environmental Materials.* 2023; 6: e12340.
[15] T. Le, N. Sadique, L. M. Housel, A. S. Poyraz, E. S. Takeuchi, K. J. Takeuchi, A. C. Marschilok, P. Liu. Discharging behavior of hollandite α-MnO_2 in a hydrated zinc-ion battery. *ACS Applied Materials & Interfaces.* 2021; **13**: 59937-59949.
[16] T. Le, E. S. Takeuchi, K. J. Takeuchi, A. C. Marschilok, P. Liu. Tuning discharge behavior of hollandite α-MnO2 in hydrated zinc ion battery by transition metal substitution. *The Journal of Physical Chemistry C.* 2023; **127**: 907-918.
[17] S.-Z. Yang, K. R. Tallman, P. Liu, D. M. Lutz, B. Zhang, S. J. Kim, L. Wu, A. C. Marschilok, E. S. Takeuchi, K. J. Takeuchi, Y. Zhu. The effects of vanadium substitution on one-dimensional tunnel structures of cryptomelane: Combined TEM and DFT study. *Nano Energy.* 2020; **71**: 104571.
[18] M. H. Alfaruqi, J. Gim, S. Kim, J. Song, J. Jo, S. Kim, V. Mathew, J. Kim. Enhanced reversible divalent zinc storage in a structurally stable α-MnO_2 nanorod electrode. *Journal of Power Sources.* 2015; **288**: 320-327.
[19] B. Lee, H. R. Lee, H. Kim, K. Y. Chung, B. W. Cho, S. H. Oh. Elucidating the intercalation mechanism of zinc ions into α-MnO_2 for rechargeable zinc batteries. *Chemical communications.* 2015; **51**: 9265-9268.

[20] B. Lee, C. S. Yoon, H. R. Lee, K. Y. Chung, B. W. Cho, S. H. Oh. Electrochemically-induced reversible transition from the tunneled to layered polymorphs of manganese dioxide. *Scientific reports.* 2014; **4**: 1, 6066.
[21] W. Sun, F. Wang, S. Hou, C. Yang, X. Fan, Z. Ma, T. Gao, F. Han, R. Hu, M. Zhu. Zn/MnO_2 battery chemistry with H^+ and Zn^{2+} coinsertion. *Journal of the American Chemical Society.* 2017; **139**: 9775-9778.
[22] J. Huang, Z. Wang, M. Hou, X. Dong, Y. Liu, Y. Wang, Y. Xia. Polyaniline-intercalated manganese dioxide nanolayers as a high-performance cathode material for an aqueous zinc-ion battery. *Nature communications.* 2018; **9**: 2906.
[23] Q. Zhao, X. Chen, Z. Wang, L. Yang, R. Qin, J. Yang, Y. Song, S. Ding, M. Weng, W. Huang. Unravelling H^+/Zn^{2+} synergistic intercalation in a novel phase of manganese oxide for high-performance aqueous rechargeable battery. *Small.* 2019; **15**: 1904545.
[24] S. H. Kim, S. M. Oh. Degradation mechanism of layered MnO_2 cathodes in Zn/$ZnSO_4$/MnO_2 rechargeable cells. *Journal of power sources.* 1998; **72**: 150-158.
[25] S. J. Kim, D. Wu, N. Sadique, C. D. Quilty, L. Wu, A. C. Marschilok, K. J. Takeuchi, E. S. Takeuchi, Y. Zhu. Unraveling the dissolution-mediated reaction mechanism of α-MnO_2 cathodes for aqueous Zn-ion batteries. *Small.* 2020; **16**: 2005406.
[26] S. J. Kim, D. Wu, L. M. Housel, L. Wu, K. J. Takeuchi, A. C. Marschilok, E. S. Takeuchi, Y. Zhu. Toward the understanding of the reaction mechanism of Zn/MnO_2 batteries using non-alkaline aqueous electrolytes. *Chemistry of Materials.* 2021; **33**: 7283-7289.
[27] X. Zeng, J. Liu, J. Mao, J. Hao, Z. Wang, S. Zhou, C. D. Ling, Z. Guo. oward a reversible Mn^{4+}/Mn^{2+} redox reaction and dendrite-free Zn anode in near-neutral aqueous Zn/MnO_2 batteries via salt anion chemistry. *Advanced Energy Materials.* 2020; **10**: 1904163.
[28] D. Chao, W. Zhou, C. Ye, Q. Zhang, Y. Chen, L. Gu, K. Davey, S. Z. Qiao. Defect engineering of W^{6+}-doped NiO for high-performance black smart windows. *Angewandte Chemie International Edition.* 2019; **58**: 7905-7910.
[29] Y. Yuan, R. Sharpe, K. He, C. Li, M. T. Saray, T. Liu, W. Yao, M. Cheng, H. Jin, S. Wang, K. Amine, R. Shahbazian-Yassar, M. S. Islam, J. Lu. Understanding intercalation chemistry for sustainable aqueous zinc–manganese dioxide batteries. *Nature Sustainability.* 2022; **5**: 890-898.
[30] A. B. Brady, K. R. Tallman, E. S. Takeuchi, A. C. Marschilok, K. J. Takeuchi, P. Liu. Transition metal substitution of hollandite α-MnO_2: enhanced potential and structural stability on lithiation from first-principles calculation. *The Journal of Physical Chemistry C.* 2019; **123**: 25042-25051.
[31] P. Hohenberg, W. Kohn. Inhomogeneous electron gas. *Physical review.* 1964; **136**: B864-B871.
[32] W. Kohn, L. J. Sham. Self-consistent equations including exchange and correlation effects. *Physical review.* 1965; **140**: A1133-A1138.
[33] G. Kresse, J. Hafner. Ab initio molecular-dynamics simulation of the liquid-metal–amorphous-semiconductor transition in germanium. *Physical Review B.* 1994; **49**: 14251-14269.
[34] G. Kresse, J. Furthmüller. Efficiency of ab-initio total energy calculations for metals and semiconductors using a plane-wave basis set. *Computational materials science.* 1996; **6**: 15-50.
[35] P. E. Blöchl. Projector augmented-wave method. *Physical review B.* 1994; **50**: 17953-17979.
[36] J. P. Perdew, K. Burke, M. Ernzerhof. Generalized gradient approximation made simple. *Physical review letters.* 1996; **77**: 3865-3868.
[37] S. Liu, M. G. White, P. Liu. Mechanism of oxygen reduction reaction on Pt (111) in alkaline solution: importance of chemisorbed water on surface. *The Journal of Physical Chemistry C.* 2016; **120**: 15288-15298.
[38] H. J. Monkhorst, J. D. Pack. Special points for Brillouin-zone integrations. *Physical review B.* 1976; **13**: 5188-5192.

[39] M. Kaltak, M. Fernández-Serra, M. S. Hybertsen. Charge localization and ordering in $A_2Mn_8O_{16}$ hollandite group oxides: Impact of density functional theory approaches. *Physical Review Materials.* 2017; **1**: 075401.
[40] N. Yamomoto, T. Endo. Single crystal growth of α-MnO_2. *Japanese Journal of Applied Physics.* 1974; **13**: 723.
[41] J. Shin, D. S. Choi, H. J. Lee, Y. Jung, J. W. Choi. Hydrated intercalation for high-performance aqueous zinc ion batteries. *Advanced Energy Materials.* 2019; **9**: 1900083.
[42] A. Urban, D.-H. Seo, G. Ceder. Computational understanding of Li-ion batteries. *npj Computational Materials.* 2016; **2**: 1-3.
[43] G. Henkelman, A. Arnaldsson, H. Jónsson. A fast and robust algorithm for Bader decomposition of charge density. *Computational Materials Science.* 2006; **36**: 354-360.
[44] E. Sanville, S. D. Kenny, R. Smith, G. Henkelman. Improved grid-based algorithm for Bader charge allocation. *Journal of computational chemistry.* 2007; **28**: 899-908.
[45] W. Tang, E. Sanville, G. Henkelman. A grid-based Bader analysis algorithm without lattice bias. *Journal of Physics: Condensed Matter.* 2009; **21**: 084204.
[46] M. Yu, D. R. Trinkle. Accurate and efficient algorithm for Bader charge integration. *The Journal of chemical physics.* 2011; **134**: 064111.